Materials & Design 213 (2022) 110322

Contents lists available at ScienceDirect

Materials & Design

journal homepage: www.elsevier.com/locate/matdes

Mechano-electrochemical phase field modeling for formation and modulation of dendritic Pattern: Application to uranium recovery from spent nuclear fuel

Chen Lin [a,*], Kui Liu [a], Haihui Ruan [b,*], Biao Wang [a,c]

[a] Sino-French Institute of Nuclear Engineering and Technology, Sun Yat-Sen University, Zhuhai, China
[b] Department of Mechanical Engineering, The Hong Kong Polytechnic University, Hong Kong, China
[c] School of Physics, Sun Yat-Sen University, Guangzhou, China

HIGHLIGHTS

- Mechano-electrochemical phase-field model is developed to tackle effects concentration, electric and stress fields and interfacial anisotropy in molten-salt electrorefining.
- The role of plating stress on the dendric growth is firstly considered.
- Dendrite patterns can be needle-like, tooth-like, or tree-like, which are consistent with experimental observations and quantitively demarcated based on the perimeter-to-area ratio.
- The coupling effects of applied voltage, molten-salt diffusivity and plating stress on dendritic growth are investigated and quantified in parametric diagrams.

GRAPHICAL ABSTRACT

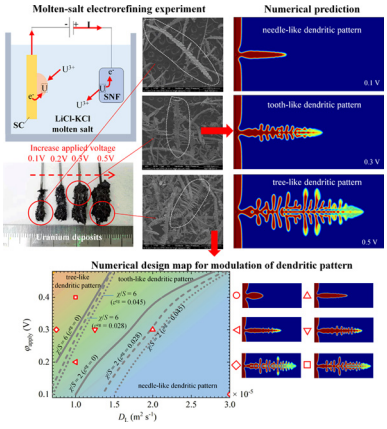

ARTICLE INFO

Article history:
Received 26 September 2021
Revised 10 December 2021
Accepted 11 December 2021
Available online 18 December 2021

Keywords:
Phase field modeling
Dendritic formation and modulation
Mechano-electrochemical coupling

ABSTRACT

Dendrite formation is a critical issue in uranium recovery from spent nuclear fuel (SNF) through a molten-salt electrorefining process. To understand and modulate uranium dendritic formation, we developed a computation model that involves all the complexities in the mechano-electrochemical process, such as diffusion–reaction kinetics, interfacial anisotropy and the variations of electric and stress fields. In particular, the lattice mismatch between deposit and substrate is considered which addressed the importance of cathode material. The model explains various morphologies of dendrites, which in a two-dimensional scenario can be demarcated based on the perimeter-to-area ratio, χ/S. Dendrites can be needle-like, tooth-like, or tree-like when $\chi/S < 2$ mm^{-1}, 2 mm$^{-1} \leq \chi/S < 6$ mm^{-1}, and $\chi/S \geq 6$ mm^{-1}, respectively. With these conditions, the parameter maps for modulating dendritic patterns are drawn to elucidate the effects of interfacial anisotropy, nuclei site geometry, diffusivity, electric and stress fields, which can be employed to design a molten-salt electroplating process to minimize failures caused by dendrite formation.

* Corresponding authors.
E-mail addresses: linch67@mail.sysu.edu.cn (C. Lin), haihui.ruan@polyu.edu.hk (H. Ruan).

https://doi.org/10.1016/j.matdes.2021.110322
0264-1275/

1. Introduction

Currently, 442 operating nuclear reactors in the world are providing over 2700 TWh of electricity or 10% of global electricity [1]. They have been regarded as one of the solutions to energy crisis and carbon neutrality owing to the abundance of the fissile/fissionable materials. However, nuclear plants do create their own waste in the form of highly radioactive spent nuclear fuel (SNF), which has accumulated to over 0.4 million metric tons of heavy metal (tHM) throughout the world as of 2017 [2]. Since SNF continues emitting high-level of radiation for thousands of years, its long-term management faces significant challenge and uncertainty. This intensifies the need to develop novel approaches to process SNF before storage or disposal.

Pyroprocessing has been regarded as one of the most potential and effective method to solve SNF issue. Among others, molten-salt electrorefining is the most representative technique firstly developed by Argonne National Laboratory [3]. In this process, SNF is anodically dissolved into molten chlorides; then, most of uranium and a small amount of actinides mixture are electrodeposited onto a solid cathode (SC) and a liquid cadmium cathode (LCC), respectively. However, the uncontrolled growth of uranium dendrite causes short circuit of an electrolytic cell. This problem occurs unpredictably even when scrapers are used to remove dendrites at constant time intervals because the growth of a dendrite could be very rapid. According to Ref. [4], the growth rate is approximately 70 $\mu m\ s^{-1}$ when the gradient of applied voltage is 10 $kV\ m^{-1}$ at 773 K. Dendrite growth restricts the continuous and efficient operations of molten-salt electrorefining, thus stopping it from large-scale applications. Therefore, understanding and predicting the growth of uranium dendrite during electrodeposition become essential for the industrial-scale apparatus design of actinide recovery.

The very first experimental step to obtain uranium dendrites can be traced back to 1953 at The University of Chicago, Marzano and Noland [5] attempted to electro-refine natural uranium by a constant current electrolysis in fused salt baths composed of various eutectics of alkali metal chlorides. They obtained uranium dendrites under a specific condition but lacked experimental conditions to explore factors affecting the growth of uranium dendrites. In 1964, Campbell and Sullivan [6] made a progress to explore and compare the macroscopic dendritic deposits under different cell voltage range from 0.12 to 0.30 V. Later in 1988, Marshall *et al.* [7] developed a potential- and current-pulse technique to eliminate dendrites, aiming at plate thick, metallurgically sound uranium bodies with specified geometries for special nuclear applications. In recent years, as countries pay more attention to the pyroprocessing of SNF, many works were done to consider the influence of multi-component complex molten salt systems and different electrochemical conditions on the growth of uranium dendrites. In general, factors observed having impact on the appearance of uranium deposition either from experiments include molten salt composition [4,6,8–11], temperature [10,12], cathode material [12–14], electrolysis technique and impurity [7,12,15,16,17].

While experimental investigation is very difficult or almost impossible to quantitatively analyze the growth process of uranium dendrites. In addition, many influencing factors observed in a complex system, which also make a challenge to distinguish the key factor on the growth of uranium dendrites from an experimental perspective. Therefore, the theoretical and numerical studies have been conducted to reveal the mechanism. Most of the existing models for dendritic formation during electrodeposition followed the studies of Barton and Bockris [18], who formulated a convexity-induced increase in diffusion flux and assumed a constant rate of reduction kinetics. Thus, the faster deposition rate at protrusion tips—which can be assumed to be hemispherical—leads to dendrites. Similarly, considering a diffusion-mediated cathodic electrodeposition process, Aogaki and Makino [19] found that surface roughening always occurred whatever how large a surface energy was. Under a high current or electropotential, Chazalviel [20] found that a dendrite growth was induced by the localized deviation from the electroneutrality which is the consequence of cation depletion near the electrode during electrodeposition.

Dendrite growth is also the critical issue limiting the capacity of rechargeable batteries [21,22,23]. It causes short circuit in lithium-metal batteries, which has prevented them from commercial applications since their advent in the 1970s [24]. Monroe and Newman [25] employed the Butler–Volmer (BV) equation to formulate a curvature-dependent electrodeposition kinetics that incorporated the effect of elastic or elastoplastic deformation. They later extended the model to account for the effect of mechanical pressure and evaluated the effectiveness of using bulk solid electrolyte to block dendrite growth [26,27]. Haataja *et al.* [28] studied the effect of electrolyte additives on the dendritic formation based on a perturbation model. Considering that lithium is a soft metal that deforms easily, Yamaki *et al.* [29] employed a fluid-dynamics model to describe the interfacial dynamics between two pressurized fluids and to investigate the effects of surface tension and mechanical pressure. Mayers *et al.* [30] and Aryanfar *et al.* [31] developed a Monte Carlo model wherein the probability determining whether cations depositing onto the electrode tip or valley was assumed to be a function of free energy change. These models dealt with the conditions causing growth instability based on a fixed electrode – electrolyte interface; however, the complex morphology evolution was not revealed.

Nielsen *et al.* [32] and Liu *et al.* [33] later proposed numerical models to simulate a continuous dendrite growth with the assumption of sharp interfaces. To deal with the deposit-electrolyte interface migration during an electrochemical process, they employed an interface tracking algorithm and a remeshing or moving-mesh technique. These approaches are however quite difficult to extend to complex problems involving, e.g., interface brunching or merging. Introducing a diffusive interface, the phase field (PF) method replaces the complicate interface-tracking issue with the variations of phase identities which are field variables that varies continuously across interfaces. Owing to the simplicity, PF method becomes very popular in studying microstructure or morphology evolutions. For dendric growth, Guyer *et al.* [34,35] made the earliest attempts. They assumed a constant electrochemical reaction rate and employed the Allen-Cahn equation to govern the decrease in the total free energy of the system. Later, Shibuta *et al.* [4,36] employed the similar formulae to study the electrochemical deposition in pyroprocessing SNF, namely, the uranium dendrite growth on a SC. Noting that electrodeposition system is generally a nonequilibrium process especially under a charging voltage, Bazant and his coworkers [37–39], Cogswell [40], Chen and his coworkers [41 –43], and Hong *et al.* [44,45], developed the so-called nonlinear electrochemical PF models, in which the equation governing interfacial migration reconciles the total free energy minimization and the BV electrochemical reaction kinetics. Nonliquid (crystalline or glassy) electrolytes can provide mechanical resistance in the form of compressive stress to dendrite growth. For example, Harry *et al.* [46] experimentally observed that the growth rate of dendrite was significantly reduced by an order of magnitude when the solid electrolyte has a sufficient elastic modulus. Therefore, it is necessary to couple electrochemical and mechanical processes in a PF model, such as those developed by

Yurkiv *et al.* [47,48] as well as Jana *et al.* [49,50]. In the study of Jana *et al.* [50], a mechano-electrochemo PF model was developed to reveal the effects of surface tension and elastoplastic deformation on electrodeposition. They exhibited six distinct regimes of lithium growth, namely, thermodynamic suppression regime, incubation regime, base-controlled growth regime, tip-controlled growth regime, mixed growth regime, and the Sand's regime [51].

Despite the aforementioned efforts in understanding dendrite growth, seldomly considered is the effect of plating stresses—caused by the lattice mismatch between deposition and cathodic electrode—on the dendrite formation and morphology evolution. Recently, Wang *et al.* [52] suggested a soft SC scaffold for lithium plating to achieve higher coulombic efficiency and capacity retention because they confirmed experimentally the role of plating stresses in dendrite formation through depositing lithium on soft substrate; that is, the dendric growth can be mitigated with a soft substrate through interface-wrinkling-induced stress relief. Therefore, the role of plating stress needs further investigation in other electrodeposition processes, such as the molten-salt electrorefining concerned in this work. Moreover, to the best of our knowledge, a numerical model of molten-salt electrorefining has not been available to describe all the complexities of electrochemical and mechanical processes and their intrinsic interaction and to explain the different experimental observations in the course uranium dendritic formation.

Thus, the present work establishes a PF model to tackle the complicated mechano-electrochemical coupling in the molten-salt electrorefining. We employed a generalized Butler-Volmer equation to describe the electrodeposition kinetics and expressed the free energy of the system as the sum of chemical potential, interfacial energy, electrostatic potential energy, and mechanical strain energy. The proposed model deals with the effects of reaction kinetics, diffusivity, interfacial anisotropy, electric and stress fields. In particularly, the platting stresses induced by the lattice mismatch between the deposit and SC is involved in the PF model of dendritic growth for the first time, which exhibits a significant effect, consistent with existing experiment results [53 54]. The model reveals the mechanism of dendrite growth and provides a quantitative explanation of experimentally observed dendritic patterns. The theoretical model can be a powerful tool in designing a molten-salt electroplating process as it guides the determinations of applied voltage, diffusivity, and substrate material to modulate dendritic patterns and inhibit dendrite growth. As such, the risk of short circuit of an electrolytic cell caused by the uncontrolled dendritic growth of uranium will be better managed.

2. Methodology

2.1. Uranium electrodeposition experiment

The present study focuses on a voltage-controlled uranium electrolysis in LiCl-KCl (51:49 mol%) molten salt at 773 K. Fig. 1 (a) shows schematically an electrorefining process, where SNF is anodically dissolved into the LiCl-KCl molten salt under an external electric potential. On the SC, the uranium cations, U^{3+}, are reduced to form uranium deposits:

$$U^{3+} + 3e^- \rightarrow U. \tag{1}$$

The experimental set-up we have established for the molten-salt electrochemistry is a high temperature electrochemical cell consisting a corundum crucible of 50 × 100 mm placed in a stainless-steel tank welded in a glove box countertop and heated by a programmable electric furnace, as shown in Fig. 1(b). After electrolysis tests lasting for 300 s, a clear increase in the outer size of uranium deposits resulting from the increase in applied voltage from 0.1 to 0.5 V were observed, as shown in Fig. 1(c). The zoom-in image of uranium deposits shown in Fig. 1(d), obtained using a scanning electron microscope (Quanta 400 FEG), exhibits a typical tree-like dendritic pattern under the applied voltage of 0.5 V.

2.2. Mechano-electrochemical coupled phase field modeling

Let us focus on the uranium electrodeposition taking place at the SC and model the cathodic reaction (Eq. (1)) using the PF approach. We follow Chen *et al.* [42] to assume that the electrolyte is the ideal dilute solution and electrons are sufficiently supplied to the dendrite surface through the circuit. Additionally, the mechanical deformation induced by the lattice mismatch between deposition and SC is involved in present model, which does affect the dendrite growth as shown in the later part of this article.

The governing equation of the electrodeposition can be expressed as (see Appendix A for derivation):

$$\frac{\partial\phi}{\partial t} = -L_{\text{int}}\left(W\frac{\partial g(\phi)}{\partial\phi} - s_0\delta_0\left(\eta^2\nabla^2\phi - \frac{\partial}{\partial x}\left(\eta\frac{\partial\eta}{d\theta}\frac{\partial\phi}{\partial y}\right) + \frac{\partial}{\partial y}\left(\eta\frac{\partial\eta}{d\theta}\frac{\partial\phi}{\partial x}\right)\right)\right) + \frac{\partial h(\phi)}{\partial\phi}L_{\text{bulk}}\left(\frac{c_{U^{3+},L}}{c^{\text{ref}}_{U^{3+},L}}\exp\left(\frac{(1-\rho)\left(\mu_R^{\text{ex}}-\mu_P^{\text{ex}}\right)}{RT}\right) - \phi\exp\left(-\frac{\rho\left(\mu_R^{\text{ex}}-\mu_P^{\text{ex}}\right)}{RT}\right)\right) \tag{2}$$

with the symbols defined as follows.

$\phi \in [0, 1]$ is the order parameter associated with the concentration of atomic uranium in deposit, $c_{U,S}$, and its reference value, $c^{\text{ref}}_{U,S}$, as $\phi = c_{U,S}/c^{\text{ref}}_{U,S}$(namely, it describes the spatial distribution of deposit (ϕ = 1) and electrolyte (ϕ = 0) phases).

$g(\phi) = \phi^2(1\text{-}\phi)^2$ is a double-well function to ensure that both deposit and electrolyte phases are stable with the prefactor W being the energy barrier.

$h(\phi)$ is an interpolation function in the form of $h(\phi) = \phi^3\,(10 - 15\phi + 6\phi^2)$ [54] that varies from one to zero across the interface to mollify the material discontinuity across the deposition-electrolyte interface; accordingly, $\partial h(\phi)/\partial\phi$ is to ensure that the reaction only takes place at a deposit-electrolyte interface.

η is an orientation-dependent parameter to scale the anisotropy of interfacial energy and thickness. If θ is the angle between normal direction of interface and the nominal axis of growth, for a two-dimensional case, it is expressed that $\eta = 1 + \gamma\cos(k(\theta - \theta_0))$ [56], where γ is the strength of interfacial anisotropy, θ_0 represent the fastest growth direction of dendrite and k specifies the mode number that would be set as k = 4, because the Uranium lattice has a cubic structure [56].

Other parameters in Eq. (2) are: μ_R^{ex} and μ_P^{ex}, the excess chemical potentials of reactants and products, respectively, L_{int} and L_{bulk}, the coefficients to scale the contributions of the interface energy and the deposition kinetics to phase migration, respectively, s_0 and δ_0, the interfacial energy density (per unit area) and interfacial thickness, respectively, $c_{U^{3+},L}$ and $c^{\text{ref}}_{U^{3+},L}$, the concentration of uranium cation in electrolyte phase (L) and its reference (saturated) value, respectively, ρ a constant between zero and one, known as the asymmetry parameter [55] to define the transition state in an electrochemical reaction, R and T, the ideal gas constant and thermodynamic temperature, respectively.

For the concerned electrochemical deposition (Eq. (1)), the chemical potential difference, $\mu_R^{\text{ex}} - \mu_P^{\text{ex}}$, as well as the coefficients L_{int} and L_{bulk} can be expressed as:

$$\begin{aligned}\mu_R^{\text{ex}} - \mu_P^{\text{ex}} = {} & \mu^0_{U^{3+},L} - \mu^0_{U,S} - nF(\varphi_S - \varphi_L) \\ & - \frac{\partial h(\phi)}{2c^{\text{ref}}_{U,S}\partial\phi}\left(\boldsymbol{\varepsilon} - h(\phi)\boldsymbol{\varepsilon}^g\right)^T\cdot\boldsymbol{D}^e_S\left(\boldsymbol{\varepsilon} - h(\phi)\boldsymbol{\varepsilon}^g\right), \\ & - \frac{h(\phi)}{c^{\text{ref}}_{U,S}}\left(\boldsymbol{\varepsilon} - h(\phi)\boldsymbol{\varepsilon}^g\right)^T\cdot\boldsymbol{D}^e_S\left(\frac{\partial\boldsymbol{\varepsilon}}{\partial\phi} - \frac{\partial h(\phi)}{\partial\phi}\boldsymbol{\varepsilon}^g\right)\end{aligned} \tag{3a}$$

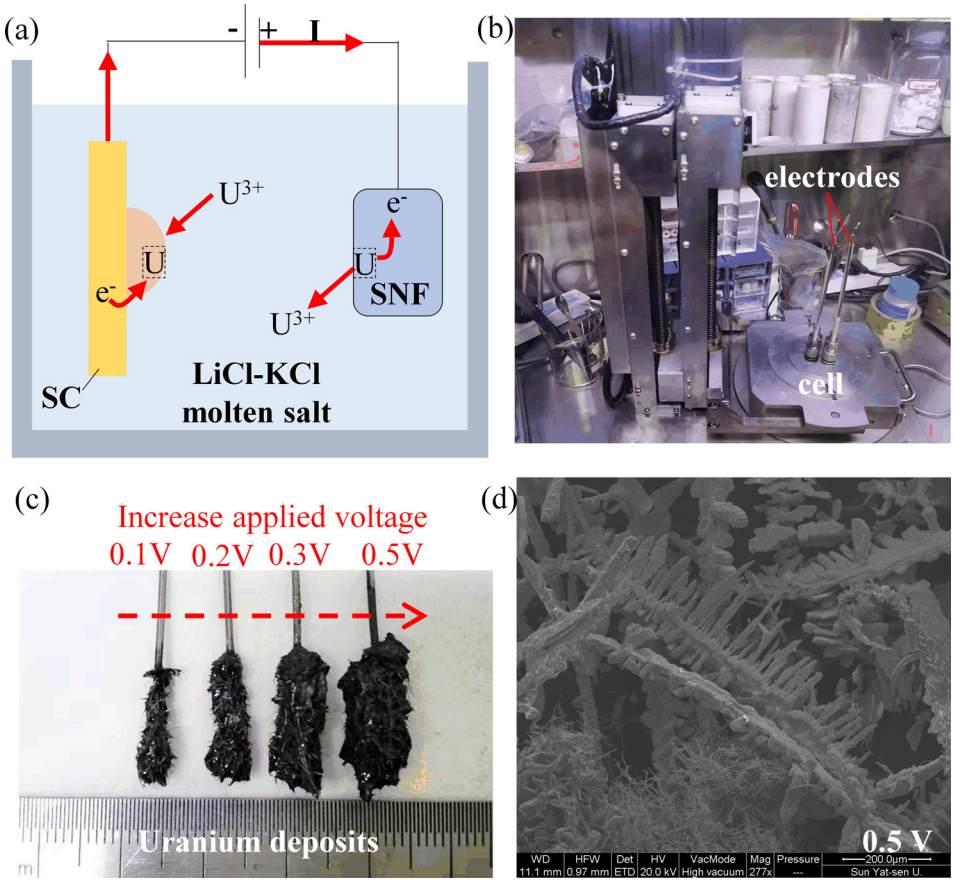

Fig. 1. Experiments of molten-salt electrorefining: (a) schematic of the electrochemical system, (b) the experimental set-up for the molten salt electrochemistry, (c) uranium deposits detached from the cathode for different applied voltage of 0.1 V, 0. 2 V, 0.3 V and 0.5 V after electrodeposition of 300 s at 773 K, and (d) the representative SEM images of uranium dendrites with applied voltage of 0.5 V.

$$L_{int} = \frac{k_0}{a_{TS}\left(c^{ref}_{U,S}\right)^{2}RT}\exp\left(-\frac{\rho\left(\mu^0_{U^{3+},L}-\mu^0_{U,S}-nF(\varphi_S-\varphi)\right)}{RT}\right)\times \exp\left(\frac{\rho\partial\left((\boldsymbol{\varepsilon}-h(\phi)\boldsymbol{\varepsilon}^g)^T\cdot\boldsymbol{D}^e(\boldsymbol{\varepsilon}-h(\phi)\boldsymbol{\varepsilon}^g)\right)}{2c^{ref}_{U,S}RT\partial\phi}\right), \tag{3b}$$

and

$$L_{bulk} = \frac{k_0}{a_{TS}c^{ref}_{U,S}}. \tag{3c}$$

where $\mu^0_{U,S}$ (or $\mu^0_{U^{3+},L}$) is the standard chemical potential of uranium in the deposit (S) (or uranium cation in the electrolyte phase (L)), F is the Faraday constant, n is the charge number of a uranium cation, φ_S and φ are electrostatic potential in the metallic dendrite and electrolyte, respectively (φ_S is assume to be uniform with a constant value in the uranium dendrite as it is a conductor), k^0 is the rate coefficient, a^{TS} is the activities of the system at the reaction transition state, $\boldsymbol{\varepsilon}$ is the total strain, $\boldsymbol{\varepsilon}^{eg}$ is the mismatch eigenstrain that describes the lattice mismatch between uranium deposit and the cathodic substrate (see Appendix C), and $\boldsymbol{D}^e_S$ is the stiffness matrix of uranium. With Eq. 3, it can be observed that mechanical deformation affects dendrite growth in two ways: (*i*) it leads to a local change in electrochemical potential (Eq. (3a)) and (*ii*) it brings about interfacial instability (Eq. (3b)). The latter is also the reason that whiskers can grow from thin films under compressive stresses for stress relief [57].

The equation governing uranium (atoms and cations) diffusion can be expressed as (see Appendix A for derivation):

$$\tau\frac{\partial\mu_U}{\partial t} = \frac{D}{RT}\left(h(\phi)c^{ref}_{U,S}\exp\left(\frac{\mu_U-\mu^0_{U,S}}{RT}\right)+(1-h(\phi))c^{ref}_{U^{3+},L}\exp\left(\frac{\mu_U-\mu^0_{U^{3+},L}}{RT}\right)\right)(\nabla\mu_U+nF\nabla\varphi_L) - \frac{\partial h(\phi)}{\partial\phi}\left(c^{ref}_{U,S}-c^{ref}_{U^{3+},L}\right)\exp\left(\frac{\mu_U}{RT}\right)\frac{\partial\phi}{\partial t}, \tag{4a}$$

$$\tau = \left(h(\phi)\frac{c^{ref}_{U,S}}{RT}\exp\left(-\frac{\mu^0_{U,S}}{RT}\right)+(1-h(\phi))\frac{c^{ref}_{U^{3+},L}}{RT}\exp\left(-\frac{\mu^0_{U^{3+},L}}{RT}\right)\right)\exp\left(\frac{\mu_U}{RT}\right), \tag{4b}$$

where μ_U is the chemical potential of uranium species, D is the diffusivity of uranium species, expressed as $D = h(\phi)D_S + (1-h(\phi))D_L$ with D_S and D_L being the diffusion coefficients of uranium atom in the deposit and cation in the electrolyte, respectively. In Eq. (4a) the first term on the right-hand side governs the diffusion of uranium species due to concentration gradient and electropotential field, and the second term establishes the relation between the rate of interfacial chemical potential change, $\partial\mu_U/\partial t$, and the deposition rate, $\partial\phi/\partial t$. Note that Eq (4a) is different from those proposed by Chen and his coworkers [41 –43] and our previous works [58 – 60]. In these studies and many others, the diffusion–reaction equations govern the variation of concentrations instead of the chemical potential (i.e., the left-hand side of Eq. (4a)). The advantage of our treatment is that it avoids the problem that the concentration may become negative in numerical implementation.

For the electropotential field, φ, we assume electric neutrality in electrolyte and employ the Poisson's equation to relate with the variation rate of ϕ, given by:

$$\nabla(\varepsilon\nabla\varphi) = nFc_{U,S}^{ref}\frac{\partial\phi}{\partial t}, \tag{5}$$

where ε is the effective electric conductivity of the medium, given by $\varepsilon = \varepsilon_S h(\phi) + \varepsilon_L(1 - h(\phi))$ with ε_S and ε_L being the conductivities of the deposit and the electrolyte, respectively. The right-hand side of Eq. (5) arises from the variation of charge density resulting from the flow of electrons (e^-) into the deposition-electrolyte interface where the reduction (Eq. (1)) takes place.

3. Numerical results and discussion

In present work, we simulate two-dimensional (2D) cases for a binary-phase system consisting of uranium deposit (ϕ = 1) and molten salt electrolyte (ϕ = 0). While dendrites are three-dimensional due to perturbations from all directions, our 2D numerical model can be regarded as the scenario that the uniformity is maintained in the out-of-plane direction. This simplifica-

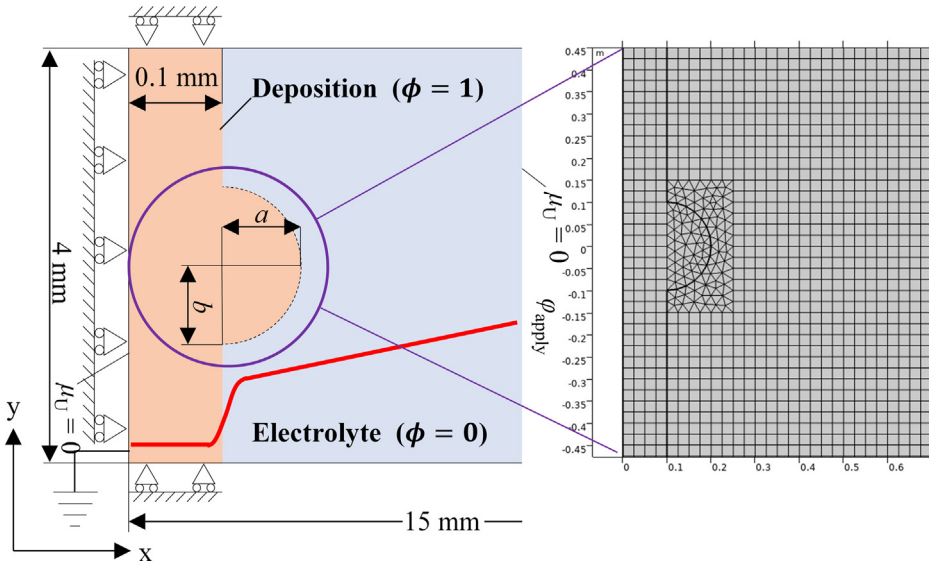

Fig. 2. The geometry and boundary conditions of the simulation domain with FE meshes.

Table 1
Parameters used in simulation.

	Parameter	Value
Reference length	l_{ref}	1 mm
Reference time	t_{ref}	1000 s
Interface thickness	δ	100 μm
interfacial energy density	s	0.5 J m^{-2}
Strength of interfacial anisotropy	γ	0.005 – 0.04
The fastest growth direction	θ_0	0
The mode number to represent the cubic structure of Uranium lattice	k	4
Young's modulus of the Uranium	E	208 GPa
Poisson's ratio of the Uranium	ν	0.23
Eigenvalue to scale lattice mismatch between deposit and substrate	ε^{eg}	0.028 – 0.045
Reference concentration of uranium	$c_{U,S}^{ref}$	79.832 mol L^{-1} (See Appendix D)
Reference concentration of uranium ion in electrolyte	$c_{U^{3+},L}^{ref}$	28.167 mol L^{-1} (See Appendix D)
Standard chemical potential of uranium	$\mu_{U,S}^{0}$	0 (See Appendix D)
Standard chemical potential of Uranium ion in electrolyte	$\mu_{U^{3+},L}^{0}$	29.191 kJ mol^{-1} (See Appendix D)
Coefficients to scale the contributions of interfacial energy to phase migration	L_{int}	2.5 × 10^{-6} m^3 J^{-1} s^{-1} [42]
Coefficient to scale the contributions of the deposition kinetics to phase migration	L_{bluk}	0.7 s^{-1} Calculated
Asymmetry factor	ρ	0.5 [42]
Diffusion coefficient of atomic uranium in solid deposition	D_S	6 × 10^{-12} m^2 s^{-1} [61]
Diffusion coefficient of ionic uranium in electrolyte	D_L	1 × 10^{-5} m^2 s^{-1} [61]
Electric conductivity of electrolyte	ε_L	1 S m^{-1} [42]
Electric conductivity of uranium deposit	ε_S	10^7 S m^{-1} [42]
Ideal gas constant	R	8.314 J mol^{-1} K^{-1}
charge number of uranium ion	n	3
Faraday's constant	F	96,485C mol^{-1}

tion allows us to run many simulations for examining the effect of key parameters and seeking possible electrochemical means to minimize dendrites. These findings should still be extendable to 3D scenarios and meaningful for experimental studies.

In Fig. 2(a) is shown the domain of simulation with the width of 15 mm, consistent with the distance of electrodes used in our experiment (Fig. 1). Along the vertical interface with the height of 4 mm is assumed a semi-elliptical hump with the axes of a = 0.05–0.3 mm and b = 0.1 mm (indicated in Fig. 1). The finite element method is employed to solve the PF equations. To guarantee the convergence of the solution, the simulation domain is discretized by employing the square mesh with a uniform element size of 0.025 mm (i.e., 1/4 interface thickness) and the triangular mesh with maximum size of 0.025 mm, as shown in Fig. 2(b). In simulation, the initial and maximum time steps are both 0.5 s (i.e., 1/2000 reference time, t_{ref}, used to make variables non-dimensionalied in simulation) for temporal integration. The parameters used in simulation are listed in Table 1.

Since the chemical potential field rather than the concentration field is solved based on Eq. (4a), the initial and boundary conditions should be given in the form of chemical potential. We assume that the deposits and electrolyte are initially at a state of chemical equilibrium, therefore $\mu_U = 0$ at $t = 0$. The corresponding equilibrium concentrations of uranium atoms in the deposit and cations in the electrolyte is then determined to be 79.832 and 0.3 mol·L^{-1}, respectively (see Appendix B). Also, chemical equilibrium is assumed in the far-field, i.e. a Dirichlet boundary condition, $\mu_U = 0$, is imposed on the left and right sides of the simulation domain. For top and bottom sides, the zero-flux of potential, $\nabla\mu_U = 0$, is applied to approximate periodic boundaries. For the electric field, we assume that the SC, on which the uranium deposits, is grounded, and the anode is connected to an applied voltage,

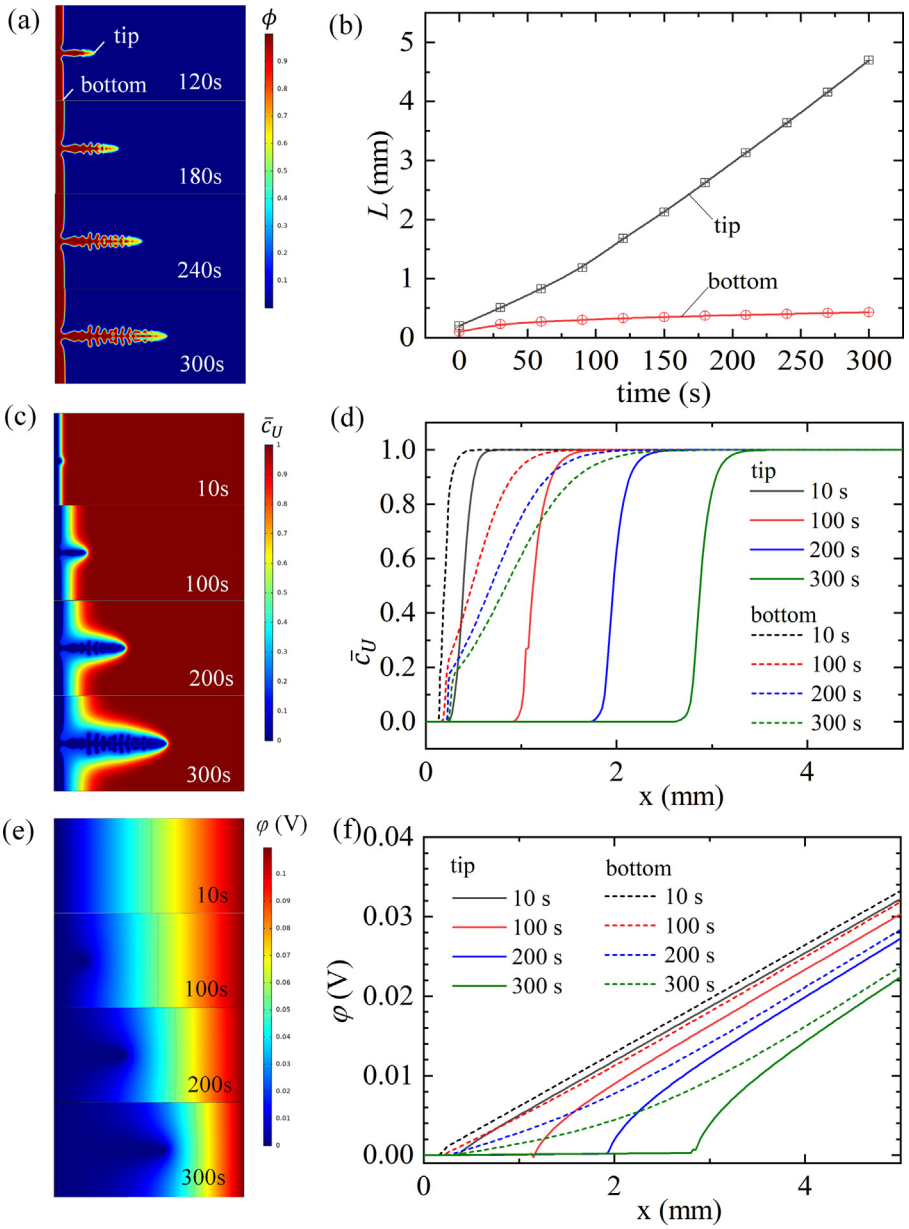

Fig. 3. Plots of a typical simulation results with an applied voltage of φ_{apply} = 0.3 V exhibiting the evolutions of (a, c, e) dendrite morphology, uranium cation concentration, and electric field, respectively, (b) the positions of dendrite tip and flat interface during electrodeposition, and (d, f) the distributions of uranium cation concentration and electropotential, respectively, along the horizontal lines passing the dendrite tip and the bottom flat interface.

φ_{apply}. Therefore, $\varphi = 0$ and $\varphi = \varphi_{apply}$ are set at the left and right sides of the calculation domain, respectively, and $\nabla\varphi = 0$ is applied to the other sides as the zero-flux condition. As for mechanical deformation, we assume that the uranium deposit is constrained by the SC; therefore, the left, top, and bottom sides are constrained along their normal direction and the right is free. The reference temperature in simulation is set at 773 K, namely the experimental condition.

3.1. Typical growth of uranium dendrite

Fig. 3(a) shows typical simulation results of how a uranium dendrite grows from a semi-elliptical hump ($a = b = 0.1$ mm) under the applied voltage of $\varphi_{apply} = 0.3$ V. It first lengthens along the opposite direction of electropotential gradient (i.e., the x direction) with the width almost unchanged, i.e., the hump first becomes a needle-like dendrite (or a whisker). After 180 s, branches are observed, i.e., the so-called hyperbranched evolution starts, causing a tooth-like pattern. By tracking the position of the main dendrite tip, the lengthening of the dendrite is plotted as the black line in Fig. 3(b), showing an accelerated growth. This kind of dendritic lengthening is one of the most dangerous scenarios in application that the uncontrolled dendrite growth leads suddenly to a sudden short circuit. In contrast, the migration of the bottom flat interface has a decelerated tendency as shown Fig. 3(b). Such a significant difference in deposition behavior is the consequence of the equations governing the evolutions of U cation concentration (Eq. (4)) and electric potential (Eq. (5)), which make them become increasingly inhomogeneous with time.

Fig. 3(c) shows that the distribution of uranium cations in the electrolyte is almost homogeneous in the early stage (e.g., first 10 s) and becomes more and more inhomogeneous with the dendrite advancing. The increase in inhomogeneity is further shown in Fig. 3(d), where the cation distributions along the horizontal lines passing the dendrite tip and away from the dendrite are exhibited. It is noted that the normalized cation concentration changes always precipitously from 0 to 1 at the tip but increasingly gently with time at the bottom; this phenomenon is easily understood considering that the protruding tip receive cations from all directions. Correspondingly, the growth instability can be reasoned that the deposition is reaction-kinetics-controlled at the tip—as the supply of cations remains unchanged—and becomes gradually diffusion-controlled at the bottom owing to the insufficient cation supply.

Because the deposition is an electrochemical process, one shall expect that the electric field becomes also more inhomogeneous with the dendrite advancing, as shown in Fig. 3(e). The distributions of electric potential along horizontal lines passing the dendritic tip and the bottom flat interface are plotted in Fig. 3(f). It is observed that at the beginning the electric potential increases linearly from the deposit-electrolyte interface to the far field. As dendrite grows, the potential gradient increases near the dendritic tip while decreases near the flat interface, finally leading to a more and more inhomogeneous electric field. Such a more and more inhomogeneous electric field drives the transport of uranium cations from the far field to the tip rather than the bottom. Also, it leads to an increase in the overpotential at the tip and a decrease at the bottom. It explains why the dendrite growth accelerates while the migration rate of the flat interface tends to vanish.

3.2. Comparations with experiments and classification of dendritic patterns

Uranium dendrite growth is further simulated with the applied voltage, φ_{apply}, varying from 0.1 to 0.5 V following our experiments (detailed experiment see supplemental material). Fig. 4(a) shows the dendritic pattern after 300 s electrodeposition under $\varphi_{apply} = 0.1$, 0.3 and 0.5 V. It is observed that with the increase in φ_{apply}, electrodeposition becomes more unstable leading to more hyperbranched evolution, i.e., the initial nucleus firstly develops into to a needle-like dendrite, then toothlike, and finally tree-like patterns, consistent with the experimental observations. In Fig. 4(b) both the experimental and simulation results of the average dendritic lengthening rate is plotted against φ_{apply} which also exhibits an excellent agreement. In Fig. 4(c), we show dendrite lengthening with time to stress that the growth is not linear but with an increasing rate especially under a high voltage. It suggests the more noncontrolled dendrite growth with the increase in applied volage, which is dangerous in industrial application.

Dendrite growth accompanies with significant changes in the area, S, and the perimeter, χ. For example, a linear increase in S may be associated with an accelerated increase in χ under the applied voltage of 0.3 V as shown in Fig. 4(d). For a whisker, the perimeter-to-area ratio, χ/S, is the reciprocal of average half width, which must be bounded as a whisker cannot become thinner with time. The increase in χ/S, when beyond a critical value, must indicate hyperbranching. Thus, χ/S is employed to quantitatively characterize the evolution of dendrite morphology. Shown in Fig. 4(e) is the variation of χ/S under different applied voltages. Note that dendrite morphologies can be classified into needle-like (whisker), tooth-like, and tree-like patterns in term of values of χ/S. The critical condition for branching happens at $\chi/S = 2$ mm^{-1} in our simulation. When $\chi/S > 2$ mm^{-1}, dendritic pattern changes from needle-like to tooth-like; the hyperbranched evolution then starts. To have a tree-like pattern, we found that $\chi/S > 6$ mm^{-1}. We also found that smaller φ_{apply} tends to inhibit hyperbranching. For example, when $\varphi_{apply} = 0.1$ V, χ/S remains less than 2 mm^{-1} and the dendrite remains needle-like in simulation. Note that experimentally, $\varphi_{apply} = 0.1$ V leads to a tooth-like pattern. We shall argue that this discrepancy indicates the effects of other factors—such as the interfacial anisotropy and lattice mismatch—which will be discussed in the following text.

Because the present PF model can describe dendrite growth in an electrodeposition process, we then proceed to address (i) how the intrinsic properties, such as nucleus geometry and interfacial anisotropy, affect dendritic formation and (ii) how to design an electrodeposition process to suppress or even avoid dendrite growth.

3.3. Effect of intrinsic properties: Nucleus geometry and interfacial anisotropy

Dendrites grow from nucleic sites and are enhanced by interfacial anisotropy. These two factors are difficult to determine in experiments; therefore, their influences may be explored by using the computation model. We have defined the elliptical nucleus (see Fig. 2) and the strength of interfacial anisotropy, γ, in our model. As the axes a and b of the elliptical nucleus are both much smaller than the width of a uranium whisker, we reckon that the sharpness a/b of the initial hump (nucleus) is more important than their individual size. In Fig. 5(a) and (b), γ-a/b maps of dendrite patters under the applied potentials of $\varphi_{apply} = 0.15$ V and $\varphi_{apply} = 0.3$ V are shown, respectively. With the conditions of $\chi/S = 2$ and 6 mm^{-1}, the maps are divided into two or three regions. When the applied potential is small, $\varphi_{apply} = 0.15$ V, the increases in γ and a/b only lead to a change from needle-like to tooth-like patterns. When the applied potential is large, $\varphi_{apply} = 0.3$ V, the more hyperbranched evolution from tooth-like to tree-like patterns with the increases in γ and a/b would be observed. Moreover, it is noted that the pattern change is more sensitive to γ than a/b; this is understandable as the nucleus geometry only influence an initial growth.

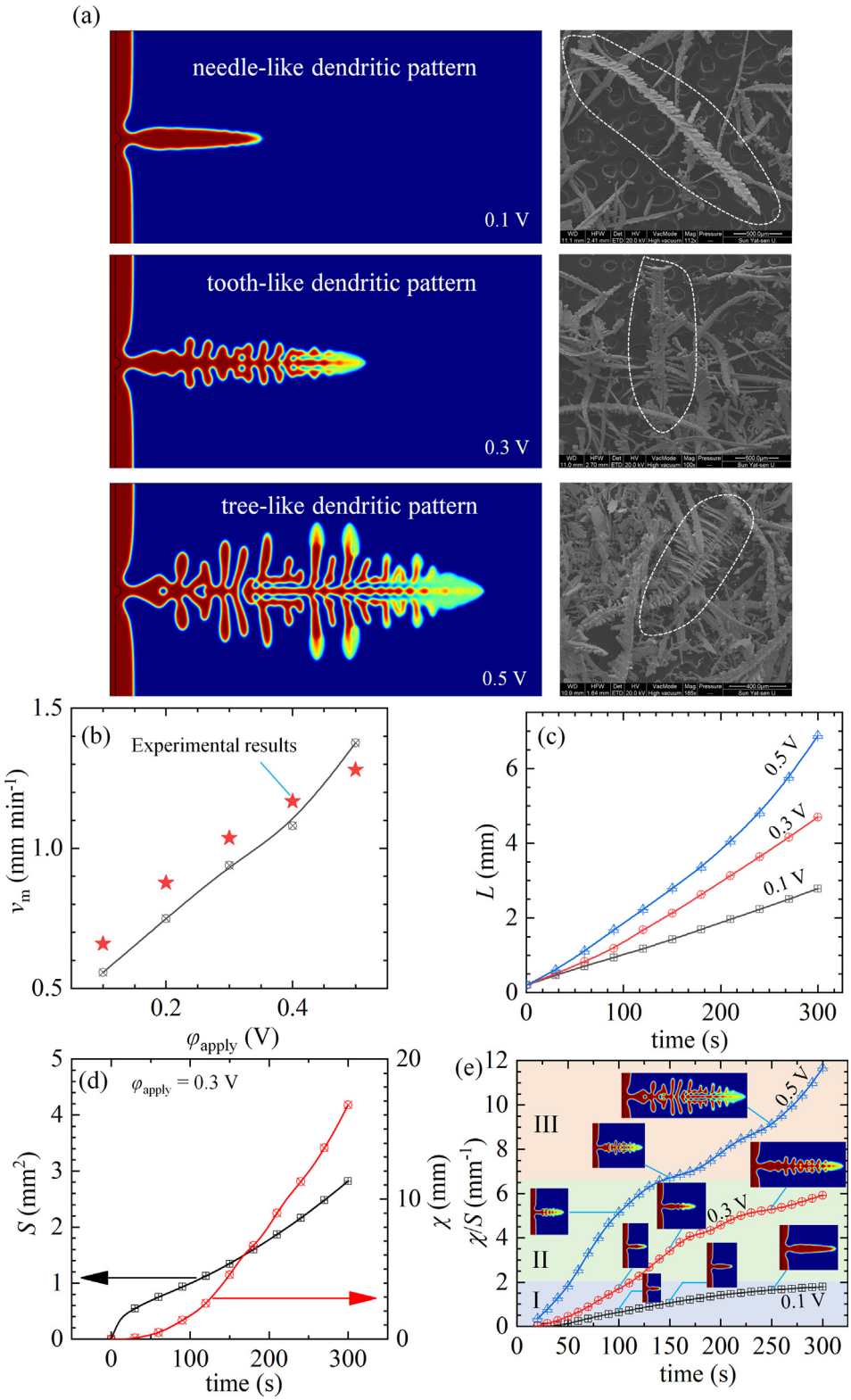

Fig. 4. Dendrite morphologies: (a) comparison of simulated and experimental dendritic patterns after the electrodeposition process of 300 s under the different applied voltage, (b) the variation of the mean velocity with applied voltage, (c) dendrite lengthening with time under different applied voltage, (d) the variations of the surface area, S, and the perimeter, χ, with time under the applied potential φ_{apply} = 0.3 V, and (e) the evolution of perimeter-to-area ratio, χ/S, with time under the different applied voltage.

3.4. Effect of plating stress and design map for suppressing dendrite growth

We have demonstrated that dendrite growth is the consequence of inhomogeneous electric and concentration fields. Here, let us add the effect of stress field induced by the lattice mismatch between deposition and electrode. It should be noted that the electric, concentration, and stress fields can somehow be adjusted through changing the applied voltage, diffusivity (e.g., through mixing other electrolytes), and SC material, respectively. However,

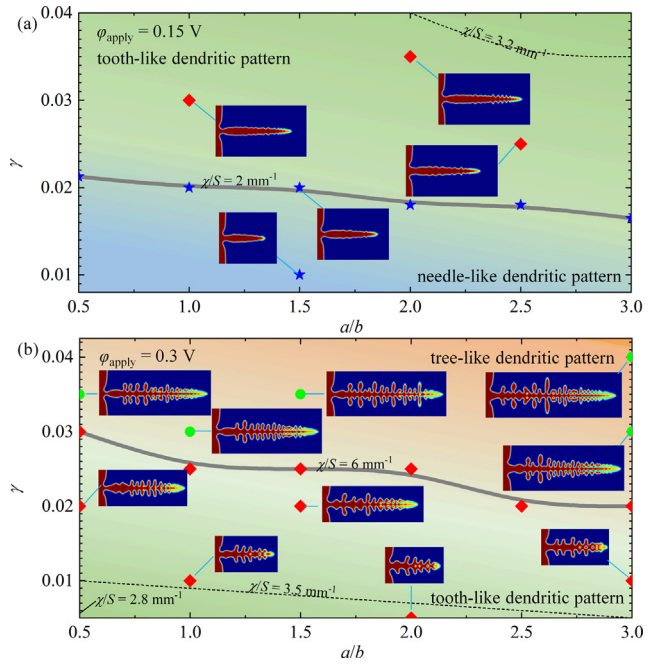

Fig. 5. Prediction maps of dendritic pattern with the variation of a/b (sharpness of a nucleus) and γ (strength of anisotropy) under the applied potentials of (a) φ_{apply} = 0.15 V and (b) φ_{apply} = 0.3 V for 300 s.

their combined effects are complicated, which cannot be clarified through experimentation only. Herein, we may conduct numerical analysis to optimize the combination these three variables to suppress or even avoid dendrite growth.

Fig. 6(a) shows the change of dendritic morphology with the variation in the applied voltage (φ_{apply} = 0.1 and 0.3 V), diffusivity (0.75 D_L, 1.5 D_L and 2 D_L), and mismatch eigenstrain (ε^{eg} = 0 and 0.028). It is observed that both the dendritic lengthening and hyperbranched evolution are significantly suppressed with the increase in diffusivity and the decrease in applied voltage and eigenstrain. With an eigenstrain and a dendrite, the resulting stress field is nonuniform, which promotes the unstable evolution of dendritic morphology. A salient result is that the dendrite becomes asymmetric as shown in Fig. 6(b).

The increase in diffusivity DL promotes the uniformity of concentration field. Therefore, an increase in the area, S, and decrease in the specific perimeter, χ, and finally the increase in the perimeter-to-area ratio, χ/S, are resulted, as shown in Fig. 6(c, d). Also, as shown in Fig. 6(c), it is noted that a stressed dendrite has smaller area and larger perimeter than the stressless counterpart does because stresses (i) decrease the reaction kinetics and thus the electrodeposition rate and (ii) induce unstable evolution of dendritic morphology. Therefore, a stressed growth has a larger perimeter-to-area ratio, χ/S, and becomes more hyperbranching. On contrary, the effect of stress can be relieved by changing the SC material with a low lattice mismatch for uranium. The similar experimental results presented by Zheng *et al.* [53] can support our numerical results. In their study, the platting stresses on dendritic growth of zinc in battery is investigated, which shows that the graphene, with a low lattice mismatch for zinc, is effective in inhibiting the growth of zinc dendrite.

Based on the proposed model and using the parameter, χ/S, to distinguish the different dendritic patterns, a design map can be drawn considering that the applied electric potential, diffusivity, and eigenstrain can be varied. This design map gives a quantitative prediction of dendrite patterns. In the bottom-right corner, the map indicates a needle-like dendrite and the simulated result is

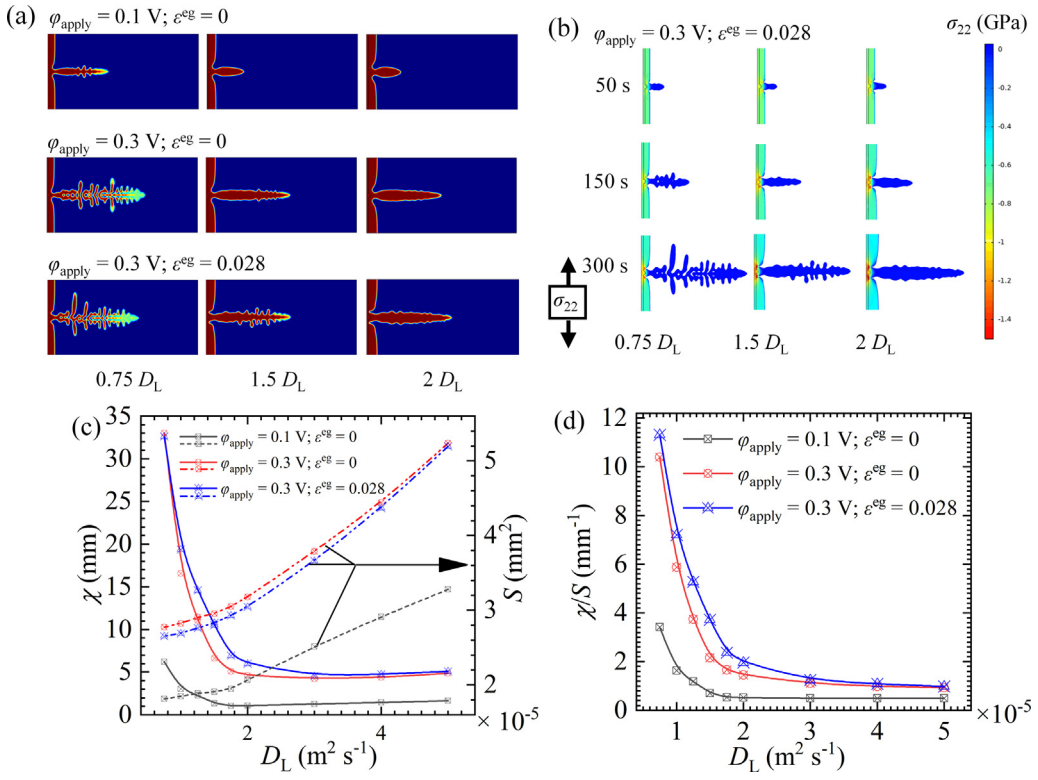

Fig. 6. The evolution of dendritic morphology with the variation in the applied voltage, φ_{apply} = 0.1 – 0.3 V, the dimensionless diffusion coefficient, 0.75D_L – 2 D_L, and the mismatch eigenstrain, ε^{eg} = 0 – 0.028, (b) the evolution of stress, σ_{22}, with different D_L and the variation of (c) the area, S, the specific perimeter, χ, and (d) the perimeter-to-area ratio, χ/S, with D_L for different values of φ_{apply} and ε^{eg}.

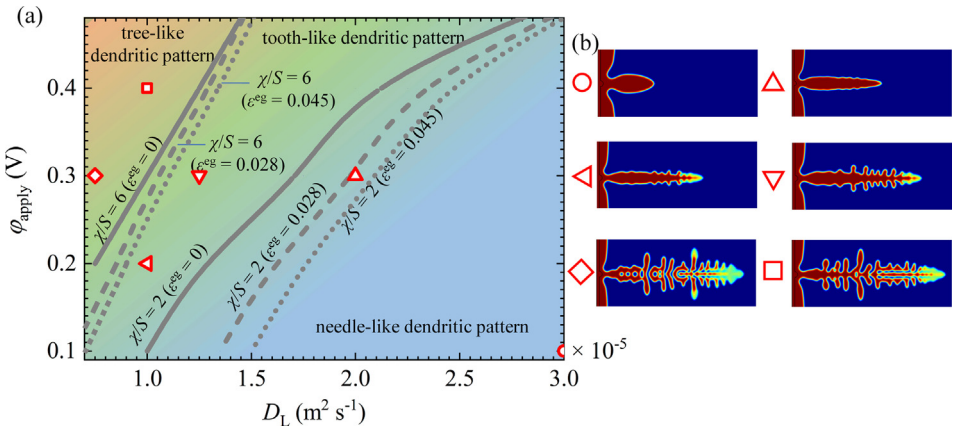

Fig. 7. Design map for different dendritic patterns with (b) examples of dendritic pattern considering that the applied electric potential, diffusivity, and eigenstrain can be varied.

more sphere-like as exemplified in Fig. 7(b). The examples of other points in the design map (Fig. 7(a)) are also shown in Fig. 7(b), showing the validity of this map. It is noted that when the eigenstrain or stresses increases, the boundary curves in the map, demarcating regions of different patterns, shift toward the lower left corner. This results in the enlargement of the regions where the dendrite tends to form the hyperbranched structures. This design map provides a useful tool to quantitatively adjust the electric, diffusive and stress fields to control or inhibit dendrite growth, which would be very meaningful for industrial application.

4. Conclusion

A new mechano-electrochemical PF model is proposed to investigate molten salt electrorefining of SNF. By employing a generalized Butler-Volmer equation to describe the electrodeposition kinetics and expressing the free energy of the system as the sum of chemical potential, interfacial energy, electrostatic potential energy, and mechanical strain energy, the PF model captures all the complexities of electrochemical and mechanical processes in an electrodepositing, such as the reaction–diffusion kinetics, interfacial anisotropy, and nonuniform electric and stress fields. The proposed model describes uranium dendrite growth and leads to the following findings.

The hyperbranched growth, manifested by the increase in the level of branches with the increase in the applied voltage, is consistent with the experimental observation. Associated with the dendrite formation, the accelerated lengthening of dendrite owing to the inhomogeneous distribution of concentration and electric fields have been revealed quantitively.

The perimeter-to-area ratio, χ/S, can be employed to quantitatively characterize the morphology evolution during dendrite growth. With it and the critical values at of χ/S = 2 and 6 mm^{-1}, the parametric maps with regions corresponding to needle-like, tooth-like, and tree-like morphologies can be established to access the effects of nucleus sharpness, interface anisotropy, applied voltage, diffusivity, and eigenstrain.

Eigenstrains, arising from lattice mismatch, lead to a more hyperbranched structure of dendrite because of the resulting nonuniform stress field that promotes an unstable dendritic evolution. In the potential-diffusivity map, the magnitude of eigenstrain in compression shifts the boundaries of dendritic pattern towards the lower right corner, i.e., the suppression of dendrites needs lower voltage and higher diffusivity.

Therefore, the proposed model provides a quantitate approach to predict dendrite formation, which in application may be employed to avoid the failure caused by short circuit. It is not only applicable in uranium recovery from SNF but also extendable to study similar dendrite problems in other electrochemical systems such as lithium-metal batteries.

Data Availability

The data that support the findings of this study are available from the corresponding author upon reasonable request.

Declaration of Competing Interest

The authors declare that they have no known competing financial interests or personal relationships that could have appeared to influence the work reported in this paper.

Acknowledgments

CL acknowledges the support from Guangdong Major Project of Basic and Applied Basic Research (2019B030302011), International Sci & Tech Cooperation Program of GuangDong Province (2019A050510022) and the support from Natural Science Basic Research Plan in Shaanxi Province of China (No. 2019JQ-123). KL acknowledges the National Postdoctoral Program for Innovative Talents (No. BX20180387) and the China Postdoctoral Science Foundation Grant (No. 2019M653182), the National Natural Science Foundation of China (No. 51904360). HHR acknowledges the support of the General Research Fund of the Hong Kong Research Grants Council (Grant No.: 15213619, Account code: Q73H).

Author Contribution

Assoc. Prof. Lin, Dr. Liu and Assoc. Prof. Ruan was responsible for the (1) ideation; Assoc. Prof. Lin was responsible for the (1) ideation (2) PF model establishment (3) simulation implementation (4) original-writing; Dr. Liu was responsible for the experiment; Assoc. Prof. Lin, Dr. Liu, Assoc. Prof. Ruan and Prof. Wang was responsible for the manuscript (1) discussion (2) writing-review and (3) writing-editing.

Appendix A

The Helmholtz free energy of the system, Ψ, as an integral of the density functional, ψ, over the domain, Ω, is expressed as:

$$\Psi = \int_\Omega \psi dv = \int_\Omega \left(\psi^{\text{chem}} + \psi^{\text{elec}} + \psi^{\text{int}} + \psi^{\text{mech}}\right) dv. \tag{A1}$$

where ψ, is further split into four parts: ψ^{chem}, ψ^{elec}, ψ^{int}, and ψ^{mech}, which represent the chemical potential, electric potential, interfacial and mechanical energy densities, respectively.

The chemical potential density, ψ^{chem}, is constructed as a sum of the atomic uranium in deposition phase (S) and the ionic uranium in electrolyte phase (L):

$$\psi^{\text{chem}} = \left(c_{\text{U,S}} RT\left(\ln\frac{c_{\text{U,S}}}{c^{\text{ref}}_{\text{U,S}}} - 1\right) + c_{\text{U,S}}\mu^0_{\text{U,S}}\right) + \left(c_{\text{U}^{3+}\text{,L}} RT\left(\ln\frac{c_{\text{U}^{3+}\text{,L}}}{c^{\text{ref}}_{\text{U}^{3+}\text{,L}}} - 1\right) + c_{\text{U}^{3+}\text{,L}}\mu^0_{\text{U}^{3+}\text{,L}}\right), \tag{A2}$$

The electric potential energy density, ψ^{elec}, resulting from the contribution of charged ions (U^{3+}) and electrons (e^-) in system, is expressed as:

$$\psi^{\text{elec}} = F\left(n\varphi_{\text{L}} c_{\text{U}^{3+}\text{,L}} - \varphi_{\text{S}} c_{e^-}\right). \tag{A3}$$

The interfacial energy density, ψ^{int}, corresponding to the energy consumed in the creation of a unit surface of the deposition, is expressed as:

$$\psi^{\text{int}} = \frac{\lambda}{2}|\nabla\phi|^2 + Wg(\phi), \tag{A4}$$

where the first term on the right-hand side is associated with the gradient of the order parameter (or phase identification), ϕ, in a diffusive interface with a finite width, the second term gives an energy barrier to ensure that the phases on both sides of an interface are stable. The coefficients W and λ can be related to the interfacial energy density (per unit area), s, and the interfacial thickness, δ, expressed as $W = 18\ s/\delta$ and $\lambda = s\delta$ [62], respectively. Considering the orientation of uranium lattice, the interface must be anisotropic, which leads to $s = s_0\eta(\theta)$ and $\delta = \delta_0\eta(\theta)$.

The mechanical energy density is given under the assumptions of isotropy and small deformation:

$$\psi^{\text{mech}} = \frac{1}{2}\left((\boldsymbol{\varepsilon}^{\text{e}}(\phi,\boldsymbol{d}))^T \cdot (\boldsymbol{D}^{\text{e}}(\phi)\boldsymbol{\varepsilon}^{\text{e}}(\phi,\boldsymbol{d}))\right), \tag{A5}$$

where $\mathbf{D}^{\text{e}}$ and $\boldsymbol{\varepsilon}^{\text{e}}$ are the stiffness matrix and elastic strain tensor, respectively. The stiffness matrix is expressed as $\boldsymbol{D}^{\text{e}} = h(\phi)\boldsymbol{D}^{\text{e}}_{\text{S}}$ to mollify the material discontinuity across the deposit-electrolyte interface. Considering the mechanical deformation induced by the lattice mismatch between deposit and substrate, the elastic strain, $\boldsymbol{\varepsilon}^{\text{e}}$, must be expressed as:

$$\boldsymbol{\varepsilon}^{\text{e}} = \boldsymbol{\varepsilon} - h(\phi)\boldsymbol{\varepsilon}^{\text{eg}}. \tag{A6}$$

Assuming an isotropic lattice mismatch, the eigenstrain, $\boldsymbol{\varepsilon}^{\text{eg}}$, can be expressed as, $\boldsymbol{\varepsilon}^{\text{eg}} = \varepsilon^{\text{eg}}\mathbf{I}$, where $\mathbf{I}$ is the second-order identity tensor and ε^{eg} the mismatch strain (see Appendix C). In Eq. (A6) the involvement of $h(\phi)$ is also to ensure that the mechanical deformation only takes place in the solid phase.

For a generalized reaction, the reaction rate, r, can be defined as:

$$r = k^0\left(\exp\left(-\frac{\mu_{\text{TS}} - \mu_{\text{R}}}{RT}\right) - \exp\left(-\frac{\mu_{\text{TS}} - \mu_{\text{P}}}{RT}\right)\right), \tag{A7}$$

where μ_{R}, μ_{P} and μ_{TS} are the chemical potentials of reactants and products and the chemical potential at the transition state, respectively. For a reaction involving multiple reactants and products, μ_{R} and μ_{P} can be expressed as:

$$\mu_{\text{R}} = RT\ln\left(\prod_{\text{i}}\left(a_{\text{R}_\text{i}^{\text{X}_\text{i}}}\right)^{n_\text{i}}\right) + \sum_{\text{i}} n_\text{i}\mu^{\text{ex}}_{\text{R}_\text{i}^{\text{X}_\text{i}}}, \tag{A8a}$$

and

$$\mu_{\text{P}} = RT\ln\left(\prod_{\text{j}}\left(a_{\text{P}_\text{j}^{\text{Z}_\text{j}}}\right)^{m_\text{j}}\right) + \sum_{\text{j}} m_\text{j}\mu^{\text{ex}}_{\text{P}_\text{j}^{\text{Z}_\text{j}}}. \tag{A8b}$$

where denoted by R_i and P_j are reactants and products, respectively, n_i (or m_j) and X_i (or Z_j) the stoichiometric number and charge number, respectively, and a_* and μ^{ex}_* the activity and the excess chemical potential of *, respectively. According to Bazant [38], the activity is only concentration dependent, defined as:

$$a_* = \exp\left(\frac{1}{RT}\left(\frac{\delta\left(\int_\Omega\left(\psi^{\text{chem}} + \psi^{\text{int}}\right)d\omega\right)}{\delta c_*} - \mu^0_*\right)\right). \tag{A9}$$

Correspondingly, the excess chemical potential, μ^{ex}_*, is:

$$\mu^{\text{ex}}_* = \frac{\delta\left(\int_\Omega\left(\psi - \psi^{\text{chem}} - \psi^{\text{int}}\right)d\omega\right)}{\delta c_*} + \mu^0_*, \tag{A10}$$

which involves the contributions of mechanical energy, electric potential, and standard chemical potential. The chemical potential at the transition state, μ_{TS}, is defined as [38]:

$$\mu_{\text{TS}} = RT\ln a^{\text{TS}} + \rho\sum_{\text{i}} n_\text{i}\mu^{\text{ex}}_{\text{R}_\text{i}^{\text{X}_\text{i}}} + (1-\rho)\sum_{\text{j}} n_\text{j}\mu^{\text{ex}}_{\text{P}_\text{j}^{\text{Z}_\text{j}}}, \tag{A11}$$

Substituting Eqs. (A8a), (A8b), (A9), (A10), (A11) into Eq. (A7) and involving the detailed expressions of energy densities (Eqs. (A2), (A3), (A4), (A5)), the reaction rate, r, can be finally derived as:

$$r = \frac{k^0}{a^{\text{TS}}}\left(a_{\text{R}}\exp\left(\frac{(1-\rho)\left(\mu^{\text{ex}}_{\text{R}} - \mu^{\text{ex}}_{\text{P}}\right)}{RT}\right) - a_{\text{P}}\exp\left(-\frac{\rho\left(\mu^{\text{ex}}_{\text{R}} - \mu^{\text{ex}}_{\text{P}}\right)}{RT}\right)\right), \tag{A12}$$

where the activity of reactants and products, a_{R} and a_{P}, are, respectively, expressed as:

$$a_{\text{R}} = \prod_{\text{i}}\left(a_{\text{R}_\text{i}^{\text{X}_\text{i}}}\right)^{n_\text{i}} = \frac{c_{\text{U}^{3+}\text{,L}}}{c^{\text{ref}}_{\text{U}^{3+}\text{,L}}} \text{ and} \tag{A13a}$$

$$a_{\text{P}} = \prod_{\text{j}}\left(a_{\text{P}_\text{j}^{\text{Z}_\text{j}}}\right)^{m_\text{j}} = \exp\left[\frac{1}{RTc^{\text{ref}}_{\text{U,S}}}\left(W\frac{\partial g(\phi)}{\partial\phi} - s_0\delta_0\left(\begin{array}{c}\eta(\theta)^2\nabla^2\phi - \\ \frac{\partial}{\partial x}\left(\eta(\theta)\frac{\partial\eta(\theta)}{d\theta}\frac{\partial\phi}{\partial y}\right) + \frac{\partial}{\partial y}\left(\eta(\theta)\frac{\partial\eta(\theta)}{d\theta}\frac{\partial\phi}{\partial x}\right)\end{array}\right)\right)\right] + \frac{c_{\text{U,S}}}{c^{\text{ref}}_{\text{U,S}}}. \tag{A13b}$$

And the difference of excess chemical potential, $\mu^{\text{ex}}_{\text{R}}$ - $\mu^{\text{ex}}_{\text{P}}$, is expressed in Eq. (3a).

As we have defined $\phi = c_{\text{U,S}}/c^{\text{ref}}_{\text{U,S}}$ and the increase in the uranium deposition is regulated by the reaction rate r, we then follow our previous work [58 –60] to express $\partial\phi/\partial t$ in the form of $\partial\phi/\partial t = r/c^{\text{ref}}_{\text{U,S}}$, which leads to the governing equation of order parameter, ϕ, as expressed in Eq. (2).

Appendix B

We consider uranium species being uranium atoms in the deposit and uranium cations in the electrolyte. Following KKS model proposed by Kim *et al.* [63], the concentration of uranium species, c_{U}, in the interface (also in the system) is an interpolation of $c_{\text{U,S}}$ and $c_{\text{U}^{3+}\text{,L}}$:

$$c_{\text{U}} = h(\phi)c_{\text{U,S}} + (1 - h(\phi))c_{\text{U}^{3+}\text{,L}}, \tag{B1}$$

It is note that $c_{\text{U,S}}$ and $c_{\text{U}^{3+}\text{,L}}$ are not independent but related by the following equation based on KKS model [63]:

$$\frac{\partial\psi^{\text{chem}}}{\partial c_{\text{U,S}}} = \frac{\partial\psi^{\text{chem}}}{\partial c_{\text{U}^{3+}\text{,L}}} = \mu_{\text{U}}, \tag{B2}$$

i.e., the chemical potentials of uranium atom and cation are equal in the diffusive interface as they coexist. This is the so-called quasi-equilibrium condition proposed in [63], which leads to the following expressions of $c_{U,S}$ and $c_{U^{3+},L}$:

$$c_{U,S} = c_{U,S}^{ref} \exp\left(\frac{\mu_U - \mu_{U,S}^0}{RT}\right) \tag{B3a}$$

and

$$c_{U^{3+},L} = c_{U^{3+},L}^{ref} \exp\left(\frac{\mu_U - \mu_{U^{3+},L}^0}{RT}\right) \tag{B3b}$$

Because the electrochemical reaction in the interface that consumes the uranium cations and simultaneously produces uranium atoms, uranium species (either cations or atoms) must be conserved. Thus, the mass conservation law leads to the following diffusion equation of uranium species:

$$\frac{\partial c_U}{\partial t} = -\nabla \boldsymbol{j} \tag{B4}$$

where **j** is the molar flux of uranium species per unit area regulated by the gradients of chemical potential and electric fields, i.e., the Nernst-Planck equation:

$$\boldsymbol{j} = -\frac{D c_U}{RT}\left(\nabla \mu_U + nF\nabla\phi\right) \tag{B5}$$

Substituting Eqs. (B1), (B3), (B5) into Eq. (B4), the diffusion equation of uranium species can be finally expressed as Eq. (4a).

Appendix C

The reference concentration of uranium, $c_{U,S}^{ref}$, can be calculated by its molar mass, m_U = 235 g mol^{-1}, and density, ρ_U = 19.1 g cm^{-3}, as $c_{U,S}^{ref} = \rho_U/m_U$ = 79.832 mol L^{-1}. The reference concentration of uranium cation in the electrolyte, $c_{U^{3+},L}^{ref}$, is regarded as the molar concentration of eutectic mixtures of LiCl-KCl (51:49 mol %). The molar mass of LiCl-KCl (51:49 mol%) is determined as $m_{LiCl\text{-}KCl} = 0.51 m_{LiCl} + 0.49 m_{KCl}$ = 0.51 × 42.4 g mol^{-1} + 0.49 × 74.6 g mol^{-1} = 58.178 g mol^{-1}. Following Ito *et. al.* [64], the density of LiCl-KCl in 773 K is $\rho_{LiCl\text{-}KCl}$ = 1.6387 g cm^{-3}. Thus, the reference concentration of uranium cation in the electrolyte is calculated as $c_{U^{3+},L}^{ref} = \rho_{LiCl\text{-}KCl}/m_{LiCl\text{-}KCl}$ = 28.167 mol L^{-1}.

In present experiment, the mass fraction of uranium ion is 6.5 wt% of LiCl-KCl. Thus, the initial concentration of uranium ion in the molten salt electrolyte is set as $c_{U^{3+},L}^0$ = 6.5 wt%×$\rho_{LiCl\text{-}KCl}$ / m_U = 0.3 mol L^{-1}. And the initial concentration of uranium atom in deposition is set as $c_{U,S}^0 = c_{U,S}^{ref}$ = 79.832 mol L^{-1}. Since the initial chemical potential in both of deposition and electrolyte phases is set as μ_U = 0, the standard chemical potentials of uranium atom and cation can be, respectively, set as $\mu_{U,S}^0$ = 0 and $\mu_{U^{3+},L}^0$ = 29.191 kJ mol^{-1} as calculated from Eqs. (14a), (14b).

The eigenvalue, ε^{eg}, to scale the magnitude of mismatch strain can be calculated by the lattice constant of uranium, a_U = 3.7 [65], and the lattice constant of uranium of cathodic electrode materials, for example the copper (a_{Cu} = 3.6 [66]) or stainless steel ($a_{Fe\text{-}C}$ = 3.54 [67]), as $\varepsilon^{eg} = (a_U - a_{Cu})/a_{Cu} \approx 0.028$ (or $\varepsilon^{eg} = (a_U - a_{Fe\text{-}C})/a_{Fe\text{-}C} \approx 0.045$). Thus, in this simulation we set the eigenvalue as ε^{eg} = 0.028 – 0.045.

Appendix D. Supplementary material

Supplementary data to this article can be found online at https://doi.org/10.1016/j.matdes.2021.110322.

References

[1] International Energy Agency (IEA), Nuclear Power in a Clean Energy System, online edition (2019). https://www.iea.org/reports/nuclear-power-in-a-clean-energy-system.
[2] International Atomic Energy Agency (IAEA), Status and Trends in Spent Fuel and Radioactive Waste Management, online edition (2018). https://www-pub.iaea.org/MTCD/Publications/PDF/P1799_web.pdf.
[3] J.P. Ackerman, T.R. Johnson, L.S.H. Chow, E.L. Carls, W.H. Hannum, J.J. Laidler, Treatment of wastes in the IFR fuel cycle, Prog. Nucl. Energy 31 (1-2) (1997) 141–154.
[4] Y. Shibuta, S. Unoura, T. Sato, H. Shibata, M. Kurata, T. Suzuki, A phase-field simulation of uranium dendrite growth on the cathode in the electrorefining process, J. Nucl. Mater. 414 (2011) 114–119.
[5] C. Marzano, R. Noland, The Electrolytic Refining of Uranium, Argonne National Lab, Lemont, Ill, 1953.
[6] R. Campbell, T.A. Sullivan, Electrorefining Uranium in a Chloride Electrolyte, US Department of the Interior, Bureau of Mines, 1965.
[7] S.L. Marshall, L. Redey, G.F. Vandegrift, D.R. Vissers, Electroformation of uranium hemispherical shells, Argonne National Lab, IL (USA), 1989.
[8] K. Serrano, P. Taxil, O. Dugne, S. Bouvet, E. Puech, Preparation of uranium by electrolysis in chloride melt, J. Nucl. Mater. 282 (2-3) (2000) 137–145.
[9] H. Tang, Y. Du, Y. Li, M. Wang, H. Wang, Z. Yang, B. Li, R. Gao, Electrochemistry of UBr 3 and preparation of dendrite-free uranium in LiBr-KBr-CsBr eutectic melts, J. Nucl. Mater. 508 (2018) 403–410.
[10] K. Liu, J. Sun, L. Zhu, Y. Sang, W. Shi, Z. Chai, B. Wang, M. Kang, The Application of Low-Melting LiCl-KCl-CsCl Eutectic to Electrodeposit Uranium Metal, J. Electrochem. Soc. 166 (13) (2019) D606–D616.
[11] J.H. Lee, Y.H. Kang, S.C. Hwang, E.H. Kim, J.H. Yoo, H.S. Park, Separation characteristics of a spent fuel surrogate in the molten salt electrorefining process, J. Mater. Process. Technol. 189 (1-3) (2007) 268–272.
[12] K. Liu, Z. Chai, W. Shi, Uranium Dendritic Morphology in the Electrorefining: Influences of Temperature and Current Density, J. Electrochem. Soc. 165 (3) (2018) D98–D106.
[13] T. KOYAMA, M. IIZUKA, Y. SHOJI, R. FUJITA, H. TANAKA, T. KOBAYASHI, M. TOKIWAI, An Experimental Study of Molten Salt Electrorefining of Uranium Using Solid Iron Cathode and Liquid Cadmium Cathode for Development of Pyrometallurgical Reprocessing, J. Nucl. Sci. Technol. 34 (4) (1997) 384–393.
[14] C.H. Lee, T.-J. Kim, S. Park, S.-J. Lee, S.-W. Paek, D.-H. Ahn, S.-K. Cho, Effect of cathode material on the electrorefining of U in LiCl-KCl molten salts, J. Nucl. Mater. 488 (2017) 210–214.
[15] J.H. Lee, Y.H. Kang, S.C. Hwang, J.B. Shim, E.H. Kim, S.W. Park, Application of graphite as a cathode material for electrorefining of uranium, Nucl. Technol. 162 (2) (2008) 135–143.
[16] K. Liu, T. tan, X. Zhou, N. Zheng, Y. Ma, M. Kang, B. Wang, Z. Chai, W. Shi, The dendrite growth, morphology control and deposition properties of uranium electrorefining, J. Nucl. 555 (2021) 153110, https://doi.org/10.1016/j.jnucmat.2021.153110.
[17] F.R. Cattoir, T.A. Sullivan, Molten-salt Electrorefining of Uranium, US Department of the Interior, Bureau of Mines, 1964.
[18] J.L. Barton, J.O.M. Bockris, The electrolytic growth of dendrites from ionic solutions, Proc. R Soc. A: Math. Phys. Eng. Sci. 268 (1962) 485–505.
[19] R. Aogaki, T. Makino, Theory of powdered metal formation in electrochemistry—Morphological instability in galvanostatic crystal growth under diffusion control, Electrochim. Acta 26 (1981) 1509–1517.
[20] J.N. Chazalviel, Electrochemical aspects of the generation of ramified metallic electrodeposits, Phys. Rev. A 42 (1990) 7355–7367.
[21] L. Wang, S. Yin, Z. Yu, Y. Wang, T. Yue, J. Zhao, Z. Xie, Y. Li, J. Xu, Unlocking the significant role of shell material for lithium-ion battery safety, Mat. Des. 160 (2018) 601–610.
[22] G. Yang, Y. Song, Q. Wang, L. Zhang, L. Deng, Review of ionic liquids containing, polymer/inorganic hybrid electrolytes for lithium metal batteries, Mat. Des. 190 (2020) 108563, https://doi.org/10.1016/j.matdes.2020.108563.
[23] Y. Liu, H. Wei, X. Zhai, F. Wang, X. Ren, Y. Xiong, O. Akiyoshi, K. Pan, F. Ren, S. Wei, Graphene-based interlayer for high-performance lithium–sulfur batteries: A review, Mat. Des. 211 (2021) 110171, https://doi.org/10.1016/j.matdes.2021.110171.
[24] Y. Tang, L. Zhang, J. Chen, H. Sun, T. Yang, Q. Liu, Q. Huang, T. Zhu, J. Huang, Electro-chemo-mechanics of lithium in solid state lithium metal batteries, Energy Environ. Sci. 14 (2021) 602–642.
[25] C. Monroe, J. Newman, Dendrite growth in lithium/polymer systems – a propagation model for liquid electrolytes under galvanostatic conditions, J. Electrochem Soc. 150 (10) (2003) A1377, https://doi.org/10.1149/1.1606686.
[26] C. Monroe, J. Newman, The effect of interfacial deformation on electrodeposition kinetics, J. Electrochem Soc. 151 (6) (2004) A880, https://doi.org/10.1149/1.1710893.
[27] C. Monroe, J. Newman, The impact of elastic deformation on deposition kinetics at lithium/polymer interfaces, J. Electrochem Soc. 152 (2) (2005) A396, https://doi.org/10.1149/1.1850854.
[28] M. Haataja, D.J. Srolovitz, A.B. Bocarsly, Morphological stability during electrodeposition: II. Additive effects, J. Electrochem. Soc. 150 (10) (2003) C708, https://doi.org/10.1149/1.1602456.
[29] J. Yamaki, S. Tobishima, K. Hayashi, K. Saito, Y. Nemoto, M. Arakawa, A consideration of the morphology of electrochemically deposited lithium in an organic electrolyte, J. Power Sources 74 (1998) 219.

[30] M.Z. Mayers, J.W. Kaminski, T.F. Miller, Suppression of dendrite formation via pulse charging in rechargeable lithium metal batteries, J. Phys. Chem. C 116 (2012) 26214–26221.
[31] A. Aryanfar, D. Brooks, B.V. Merinov, W.A. Goddard, A.J. Colussi, M.R. Hoffmann, Dynamics of lithium dendrite growth and inhibition: pulse charging experiments and Monte Carlo calculations, J. Phys. Chem. Lett. 5 (2014) 1721–1726.
[32] C.P. Nielsen, H. Bruus, Sharp-interface model of electrodeposition and ramified growth, Phys. Rev. E 92 (2015) 042302.
[33] G. Liu, W. Lu, A model of concurrent lithium dendrite growth, SEI growth, SEI penetration and regrowth, J. Electrochem Soc. 164 (9) (2017) A1826–A1833.
[34] J.E. Guyer, W.J. Boettinger, J.A. Warren, G.B. McFadden, Phase field modeling of electrochemistry. I. Equilibrium, Phys. Rev. E 69 (2) (2004), https://doi.org/10.1103/PhysRevE.69.021603.
[35] J.E. Guyer, W.J. Boettinger, J.A. Warren, G.B. McFadden, Phase field modeling of electrochemistry. II. Kinetics. A phase-field simulation of uranium dendrite growth on the cathode in the electrorefining process, Phys. Rev. E 69 (2004).
[36] Y. Shibuta, T. Sato, T. Suzuki, H. Ohta, M. Kurata, Morphology of uranium electrodeposits on cathode in electrorefining process: A phase-field simulation, J. Nucl. Mater. 436 (2013) 61–67.
[37] T.R. Ferguson, M.Z. Bazant, Nonequilibrium thermodynamics of porous electrodes, J. Electrochem. Soc. 159 (12) (2012) A1967–A1985.
[38] M.Z. Bazant, Theory of chemical kinetics and charge transfer based on nonequilibrium thermodynamics, Acc Chem. Res. 46 (2013) 1144–1160.
[39] R.B. Smith, M.Z. Bazant, Multiphase porous electrode theory, J Electrochem. Soc. 164 (11) (2017) E3291–E3310.
[40] D.A. Cogswell, Toward Quantitative Phase-field Modeling of Dendritic Electrodeposition, Phys. Rev. E 92 (2015) 011301(R).
[41] L. Liang, L. Chen, Nonlinear phase field model for electrodeposition in electrochemical systems, Appl. Phys. Lett. 105 (2014) 1457–1459.
[42] L. Chen, H.W. Zhang, L.Y. Liang, Z. Liu, Y. Qi, P. Lu, J. Chen, L. Chen, Modulation of dendritic patterns during electrodeposition: a nonlinear phase-field model, J. Power Sources 300 (2015) 376–385.
[43] H.H. Yana, Y.H. Bie, X.Y. Cui, G.P. Xiong, L. Chen, A computational investigation of thermal effect on lithium dendrite growth, Energy Convers. Manage. 161 (2018) 193–204.
[44] Z. Hong, V. Viswanathan, Phase-Field Simulations of Lithium Dendrite Growth with Open-Source Software, ACS Energy Lett. 3 (2018) 1737–1743.
[45] Z. Hong, V. Viswanathan, Prospect of Thermal Shock Induced Healing of Lithium Dendrite, ACS Energy Lett. 4 (2019) 1012–1019.
[46] K.J. Harry, K. Higa, V. Srinivasan, N.P. Balsara, Influence of electrolyte modulus on the local current density at a dendrite tip on a lithium metal electrode, J. Electrochem. Soc. 163 (10) (2016) A2216–A2224.
[47] V. Yurkiv, T. Foroozan, A. Ramasubramanian, R. Shahbazian-Yassar, F. Mashayek, Phase-field modeling of solid electrolyte interface (SEI) influence on Li dendritic behavior, Electrochim. Acta 265 (2018) 609–619.
[48] V. Yurkiv, T. Foroozan, A. Ramasubramanian, R. Shahbazian-Yassar, F. Mashayek, The influence of stress field on Li electrodeposition in Li-metal battery, MRS Commun. 8 (3) (2018) 1285–1291.
[49] A. Jana, R.E. García, Lithium dendrite growth mechanisms in liquid electrolytes, Nano Energy 41 (2017) 552–565.
[50] A. Jana, S.I. Woo, K.S.N. Vikrant, R.E. García, Electrochemomechanics of lithium dendrite growth, Energy Environ. Sci. 12 (12) (2019) 3595–3607.
[51] P. Bai, J. Li, F.R. Brushett, M.Z. Bazant, Transition of lithium growth mechanisms in liquid electrolytes, Energy Environ. Sci. 9 (10) (2016) 3221–3229.
[52] X. Wang, W. Zeng, L. Hong, W. Xu, H. Yang, F. Wang, H. Duan, M. Tang, H. Jiang, Stress-driven lithium dendrite growth mechanism and dendrite mitigation by electroplating on soft substrates, Nat. Energy 3 (3) (2018) 227–235.
[53] J. Zheng, Q. Zhao, T. Tang, J. Yin, C.D. Quilty, G.D. Renderos, X. Liu, Y. Deng, L. Wang, D.C. Bock, C. Jaye, D. Zhang, E.S. Takeuchi, K.J. Takeuchi, A.C. Marschilok, L.A. Archer, Reversible epitaxial electrodeposition of metals in battery anodes, Sci. 366 (6465) (2019) 645–648.
[54] S.-L. Wang, R.F. Sekerka, A.A. Wheeler, B.T. Murray, S.R. Coriell, R.J. Braun, G.B. McFadden, Thermodynamically-consistent phase-field models for solidification, Physica D 69 (1-2) (1993) 189–200.
[55] A.M. Kuznetsov, J. Ulstrup, Electron Transfer in Chemistry and Biology: An Introduction to the Theory, Wiley, Chichester, U.K., 1999.
[56] J.M. Debierre, A. Karma, F. Celestini, R. Guerin, Phase-field approach for faceted solidification, Phys. Rev. E 68 (2003) 041604.
[57] E. Chason, N. Jadhav, F. Pei, E. Buchovecky, A. Bower, Growth of whiskers from Sn surfaces: driving forces and growth mechanisms, Prog. Surf. Sci. 88 (2013) 103–131.
[58] C. Lin, H. Ruan, Phase-field modeling of scale roughening induced by outward growing oxide, Mater. 5 (2019) 100255, https://doi.org/10.1016/j.mtla.2019.100255.
[59] C. Lin, H. Ruan, S.-Q. Shi, Phase field study of mechanico-electrochemical corrosion, Electrochim. Acta 310 (2019) 240–255.
[60] C. Lin, H. Ruan, S.-Q. Shi, Mechanical–chemical coupling phase-field modeling for inhomogeneous oxidation of zirconium induced by stress–oxidation interaction, NPJ. Mater. Degradation 4 (1) (2020), https://doi.org/10.1038/s41529-020-00125-6.
[61] P. Masset, D. Bottomley, R. Konings, R. Malmbeck, A. Rodrigues, J. Serp, J.-P. Glatz, Electrochemistry of Uranium in Molten LiCl-KCl Eutectic, J. Electrochem. Soc. 152 (6) (2005) A1109, https://doi.org/10.1149/1.1901083.
[62] K. Ammar, B. Appolaire, G. Cailletaud, F. Feyel, S. Forest, Finite element formulation of a phase field model based on the concept of generalized stresses, Comp. Mater. Sci. 45 (2009) 800–805.
[63] S.G. Kim, W.T. Kim, T. Suzuki, Phase-field model for binary alloys, Phys. Rev. E 60 (1999) 7186.
[64] H. Ito, Y. Hasegawa, Y. Ito, Densities of Eutectic Mixtures of Molten Alkali Chlorides below 673 K, J. Chem. Eng. Data 46 (2001) 1203–1205.
[65] B. Beeler, C. Deo, M. Baskes, M. Okuniewski, First principles calculations of the structure and elastic constants of α, β and γ uranium, J. Nucl. Mater. 433 (2013) 143–151.
[66] W.P. Davey, Precision Measurements of the Lattice Constants of Twelve Common Metals, Phys. Rev. 25 (6) (1925) 753–761.
[67] J.D. Watson, P.G. McDougall, The crystallography of widmanstätten ferrite, Acta Metallurgica 21 (1973) 961–973.